AMERICAN
METEOROLOGICAL
SOCIETY

Journal of the Atmospheric Sciences

EARLY ONLINE RELEASE

The DOI for this manuscript is doi: 10.1175/JAS-D-13-024.1

The final published version of this manuscript will replace the preliminary version at the above DOI once it is available.

If you would like to cite this EOR in a separate work, please use the following full citation:

Kurowski, M., W. Grabowski, and P. Smolarkiewicz, 2013: Towards multiscale simulation of moist flows with soundproof equations. J. Atmos. Sci. doi:10.1175/JAS-D-13-024.1, in press.

Towards multiscale simulation of moist flows with soundproof equations

Marcin J. Kurowski[1,2], Wojciech W. Grabowski[1] *
and Piotr K. Smolarkiewicz[3]

[1] *National Center for Atmospheric Research, Boulder, Colorado, USA*

[2] *Institute of Meteorology and Water Management, National Research Institute, Warsaw, Poland*

[3] *European Centre for Medium-Range Weather Forecasts, Reading, UK*

* *Corresponding author address:* Wojciech W. Grabowski, NCAR/NESL/MMM, P.O. Box 3000, Boulder, CO 80307-3000. E-mail: grabow@ncar.ucar.edu

ABSTRACT

This paper discusses incorporation of phase changes of the water substance that accompany moist atmospheric flows into the all-scale atmospheric model based on soundproof equations. Specific issue concerns developing a theoretical basis and practical implementation to include pressure perturbations associated with atmospheric circulations, from small-scale to global, into representations of moist thermodynamics. In small-scale modeling using soundproof equations, pressure perturbations are obtained from the elliptic pressure solver and are typically excluded from the moist thermodynamics. We argue that in larger-scale flows at least the hydrostatic component of the pressure perturbation needs to be included because pressure variation in synoptic weather systems may affect moist thermodynamics in a way comparable to the temperature variations. As an illustration, we consider two idealized test problems, the small-scale moist thermal rising in a stratified environment and the moist mesoscale flow over an idealized topography. We compare numerical solutions obtained with a fully-compressible acoustic-mode-resolving model and with two versions of the anelastic model, either including or excluding anelastic pressure perturbations in moist thermodynamics. The two versions of the anelastic model are referred to as the generalized and standard anelastic, respectively. In agreement with the scaling arguments, only negligible differences between anelastic and compressible solutions are simulated. Incorporation of the anelastic pressure perturbations into moist thermodynamics paves the way for future studies where larger-scale moist dynamics will be considered.

1. Introduction

Modeling the atmospheric component of the climate system, often referred to as the atmospheric general circulation, has a long history; see collection of reviews in Miller and Smolarkiewicz (2008) and Randall (2010). Because of the computational limitations, early atmospheric general circulation models (AGCMs) featured relatively low spatial resolutions (hundreds to thousands of kilometers) and were based on simplified systems of equations appropriate for the large-scale atmospheric dynamics. Nevertheless, the critical role of clouds and cloud processes for the Earth energy budget and hydrological cycle has been already appreciated in early AGCM studies (Arakawa 1975; Charney 1979). Because in early AGCMs clouds were only considered through subgrid-scale parameterizations, their representation was at best questionable. With steadily expanding computational power and increasing awareness of the limitations of cloud parameterizations — the latter sometimes referred to as the cloud parameterization deadlock (Randall et al. 2003) — the past decade witnessed developments of novel modeling approaches to better represent cloud processes in AGCMs, such as the superparameterization (Grabowski and Smolarkiewicz 1999; Khairoutdinov and Randall 2001; Randall et al. 2003) or the convection-permitting nonhydrostatic AGCM (Miura et al. 2007). The emergence of the so-called seamless weather and climate prediction paradigm (Shukla 1998, 2009; Palmer et al. 2008) is another example for appreciating the small-scale atmospheric phenomena (i.e., weather) in the climate and climate change problem.

Reducing the gridlength of AGCMs, down to the convective scale and beyond, is an example of the top-down approach, where increasingly smaller scale processes are resolved rather than parameterized through subgrid-scale modeling. However, one cannot simply reduce the AGCM gridlength to resolve small-scale processes without modifying the model equations to adequately represent the nonhydrostatic dynamics. An alternative approach where nonhydrostatic small-scale models are run applying increasingly large horizontal domains, up to the global scale, can be thought as the bottom-up approach, where cloud-scale processes are capable to feed onto progressively larger scales and thus ultimately affect global atmospheric dynamics. Experiences of the communities pursuing the top-down or the bottom-up approaches accumulate and benefit the quest for the ultimate all-scale AGCM for weather and climate research.

It may seem that the bottom-up approach is relatively straightforward as the hydrostatic dynamics (appropriate for the large-scale flows) may be thought as an asymptotic limit of the nonhydrostatic small-scale dynamics. However, the issue is more complex. Small-scale models available today do not solve generic compressible equations that are valid across the entire range of spatial scales (small-scale turbulence to global). Historically, the small-scale atmospheric models evolved along two separate paths and there is significant experience in using such models in weather-related small-scale studies. The first path consists of models built using soundproof equations (e.g., anelastic) with examples of specific models including the NCAR Clark/Hall model (Clark et al. 1996, and references therein), GFDL's Lipps and Hemler model (Lipps and Hemler 1982, 1986), French MesoNH model (http://mesonh.aero.obs-mip.fr/mesonh/) and the EULAG model (Prusa et al. 2008, and references therein). The second path consists of models originating from the compressible dynamics, for instance, the Tapp/White model (Tapp and White 1976) and the Klemp/Wilhelmson model (Klemp and Wilhelmson 1978). NCAR's Weather Research and Forecasting (WRF) Model (http://www.wrf-model.org) is a flagship example of this class of models. However, because compressible dynamics impose severe time-step limitation due to the presence of fast-propagating sound waves, atmospheric models developed based on compressible dynamics apply various techniques to limit the undesirable impact of physically-irrelevant (for weather and climate) sound waves, e.g., integrating acoustic modes with smaller timestep and low accuracy or applying implicit time integration. Systematic studies of the impact of such techniques on model solutions — for instance, when compared to fully-compressible models — especially when focusing on large-scale dynamics, are rare. We will refer to such models as elastic.

The study described in this paper builds upon the interests and recent developments in the area of soundproof systems of equations (e.g., anelastic or pseudo-incompressible). These are briefly reviewed in the next section. A key goal of this work is to progress towards moist thermodynamics valid uniformly in the context of all-scale atmospheric dynamics. Specific aspects that need to be addressed are discussed in section 3. Computational examples illustrating key points of the discussion are presented in sections 4 and 5. A brief summary and outlook in section 6 concludes the paper.

2. Modeling atmospheric circulations with soundproof equations; an overview

With higher resolution numerical weather prediction (NWP) and climate models becoming available, traditional numerical approaches face new demands. Compressible dynamics is universally valid across the entire range of spatial and temporal scales — from small-scale turbulence to planetary circulations — but impose computational limitations that are difficult to overcome; see e.g. Klein (2011). Consequently, current community efforts focus on alternative, reduced forms of the governing equations for modeling large-scale dry atmospheric motions.

An overall conclusion from the collection of works in Miller and Smolarkiewicz (2008) is that there is no set of governing equations uniformly adopted throughout the NWP community, and all operational models differ in some aspects already at the theoretical level. In spite of the ongoing debate on the preferred theoretical formulation of the governing partial differential equations (PDEs), the dominant opinion seems to be that soundproof equations are not appropriate for predicting weather and climate. On the other hand, the soundproof models progress, expand their predictive skill and range of validity, and keep attracting interests of the community. For substantiation, consider an abbreviated list of works exemplifying the community efforts. The list starts with Davies et al. (2003) that quantified departures of normal modes of atmospheric soundproof PDEs from normal modes of the fully-compressible Euler equations. Although the authors questioned the suitability of soundproof equations for weather and climate, their work in fact extended the validity of anelastic models beyond the earlier arguments of scale analyses (Ogura and Phillips 1962; Lipps and Hemler 1982). In Prusa and Smolarkiewicz (2003) and Wedi and Smolarkiewicz (2004) soundproof models were generalized to incorporate time-dependent curvilinear coordinates, thereby enabling approximations of pliant boundaries — such as finite-amplitude free surface — in soundproof equations and facilitating a coupling of nonhydrostatic anelastic and hydrostatic primitive equation models; see Wedi and Smolarkiewicz (2004) for examples. More recently, Durran (2008) generalized the pseudo-incompressible system (Durran 1989) to spatially inhomogeneous and time-dependent reference states, extending up-scale the accuracy of soundproof approximations. Concomitantly, in Abiodun et al. (2008a) and Abiodun et al. (2008b) the authors compared standard aquaplanet simulations (Neale and Hoskins 2000a,b) conducted with three different dynamical cores, including nonhydrostatic anelastic model EULAG (Prusa et al. 2008) within the framework of the Community Atmosphere Model (CAM). They reported favorable comparability of EULAG with the spectral and finite-volume hydrostatic dynamical cores, and found no evidence of inadequacy of anelastic nonhydrostatic equations for climate simulations, epitomized by the aquaplanet benchmark. More recent application of the the CAM-EULAG is reported in Abiodun et al. (2011). Arakawa and Konor (2009) proposed a hybrid system of atmospheric PDEs combining nonhydrostatic soundproof and hydrostatic primitive equations, thus paving the way for a new class of general circulation models. Using techniques of multiple-scale asymptotic analysis, Klein et al. (2010) showed a formal validity of the Durran pseudo-incompressible and the Lipps-Hemler anelastic equations for realistic magnitudes of the tropospheric potential temperature stratification, in contrast to single-scale asymptotics of Ogura and Phillips (1962) and common beliefs. Promising results from the application of an EULAG-based anelastic dynamical core to the limited area operational regional NWP model COSMO were reported recently in Ziemianski et al. (2011). On the algorithmic side, Smolarkiewicz and Szmelter (2009) and Szmelter and Smolarkiewicz (2010a,b) generalized proven conservative numerics of EULAG to fully unstructured meshes, while sustaining the accuracy of structured-grid differencing on differential manifolds. This adds yet another path to the advancement of soundproof models.

Smolarkiewicz (2011) provides a brief discussion of the numerical model EULAG and illustrates the discussion with dry simulations of idealized multiscale flow problems relevant to weather and climate. In addition, a progress towards an unstructured-mesh option of EULAG has been illustrated with simulations of atmospheric wave dynamics across a range of scales. Smolarkiewicz (2011) argues that it is difficult to find a numerical example relevant to NWP and climate studies conclusively showing a failure of soundproof approximations. The cumulative computational experience demonstrated surprising flexibility and a broader than anticipated range of validity of soundproof approximations. Nonhydrostatic soundproof equations imply non-negligible numerical advantages over fully-compressible equations, and the developments of the last decade document growing interest of the community in exploiting their strengths.

3. The moist thermodynamics in the soundproof system

The moist thermodynamics with phase changes of water substance and precipitation (rain and/or ice) impose theoretical and practical challenges that need to be addressed for the all-scale modeling of weather and climate. The extension of the moist thermodynamics to global flows — and flows for which some of the assumptions (e.g., neglecting nonhydrostatic pressure perturbations in moist simulation) may no longer be valid — is the key aspect.

On theoretical grounds, moist thermodynamics involves two issues. The first one is the latent heating associated with phase changes of the water substance. Latent heating is the key element of moist processes because it is a source of positive cloud buoyancy in otherwise stably-stratified dry atmosphere. The second issue concerns development and fallout of precipitation. Precipitation comprises a number of effects, from the impact on local buoyancy (through the condensate loading) to the impact of precipitation evaporation outside clouds and precipitation-laden downdrafts that strongly affect properties of the boundary layer. We focus here on the latent heating as its inclusion into the soundproof system brings challenges discussed below. Precipitation processes (ice processes in particular) involve representation of cloud microphysics, but its inclusion in the soundproof system is relatively straightforward.

For the ideal gas, the laws of thermodynamics allow introduction of the potential temperature $\theta = T(p_{oo}/p)^{R_d/c_p}$ as an invariant of adiabatic processes. The potential temperature is also a measure of entropy $s = c_p \ln\theta$, and it can be introduced based on entropy considerations; see discussions in Bauer (1908), Hauf and Hoeller (1987), Bryan (2008) and Pauluis (2008), among others. An important difference, however, is that entropy considerations involve assumption of the thermodynamic equilibrium which is only approximately valid for condensation and typically invalid for ice processes. Moreover, applying potential temperature as the main thermodynamic variable allows semi-implicit (i.e., implicit with respect to the fast-propagating gravity waves) formulation of the model integration scheme essential for an efficient application of the model in large-scale simulations (Smolarkiewicz et al. 2001; Grabowski and Smolarkiewicz 2002). Based on those arguments and considering that it is conserved in dry adiabatic circulations, we focus on models applying potential temperature θ as the main thermodynamic variable, in addition to mixing ratios of water substance in its various forms; cf. Grabowski (1998, 1999).

In the general case of a diabatic flow, the conservation law for the potential temperature includes the heating rate that may include contributions from radiative transfer, chemical reactions, or — the emphasis in our case — phase changes of the water substance. In the latter case, the potential temperature equation becomes:

$$\frac{d\theta}{dt} = \frac{L\theta}{c_pT}\frac{dq}{dt} \ , \tag{1}$$

where q is the appropriate water mixing ratio, L is the appropriate latent heat, and c_p is the specific heat of air at constant pressure. For the condensation, latent heating is derived through the change of the cloud water mixing ratio. In turn, this change depends on the saturation water vapor mixing ratio $q_{vs} = \epsilon e_s(T)/[p - e_s(T)] \approx \epsilon e_s(T)/p$, where $e_s(T)$ is the saturated water vapor pressure and $\epsilon = R_d/R_v$ (R_d and R_v are the gas constants for the dry air and for the water vapor, respectively). The key point is that changes of both T and p impact q_{vs}. The change of the saturated water mixing ratio Δq_{vs}, due to change of the temperature ΔT and pressure Δp, can be estimated as:

$$\Delta q_{vs} = \frac{\partial q_{vs}}{\partial e_s}\frac{de_s}{dT}\Delta T + \frac{\partial q_{vs}}{\partial p}\Delta p \ . \tag{2}$$

However, since the model predicts not the temperature T but the potential temperature θ, one needs locally convert θ into T. Such a conversion involves again pressure p and thus

$$\Delta T = \frac{\partial T}{\partial \theta}\Delta\theta + \frac{\partial T}{\partial p}\Delta p \ . \tag{3}$$

Combining (2) and (3) and using the Clausius-Clapeyron relationship for de_s/dT leads to:

$$\frac{\Delta q_{vs}}{q_{vs}} = \beta_L\frac{\Delta\theta}{\theta} - \left(1 + \frac{R}{c_p}\beta_L\right)\frac{\Delta p}{p} \ , \tag{4}$$

where $\beta_L = L/R_vT$ is a coefficient that varies between 15 and 20 for air temperatures encountered in the troposphere, and $R/c_p \approx 0.3$. Equation (4) implies that pressure perturbations have approximately an order of magnitude larger impact on q_{vs} through the conversion of θ perturbations into T perturbations [the second term in the parenthesis on rhs of (4)] than the direct effect on q_{vs} (i.e., via the denominator in q_{vs}). In particular, (4) implies that

$$\frac{\Delta q_{vs}}{q_{vs}} \sim 15\frac{\Delta\theta}{\theta} - 5\frac{\Delta p}{p} \ . \tag{5}$$

The first term on rhs of (5) represents effects of the potential temperature change on q_{vs}. In small-scale atmospheric dynamics, the temperature perturbations — or, more generally, perturbations of the density temperature that include effects of water vapor and cloud condensate on buoyancy (Emanuel 1994) — are a few degrees at most and consequently $\Delta\theta/\theta \sim 0.01$. Nonhydrostatic pressure perturbations can be estimated using several methods. For instance, the Bernoulli equation implies that the nonhydrostatic pressure perturbation (over the motionless environment) within a rising plume should vary as ρu^2. This gives pressure perturbations around 1 hPa for the velocity of $\sim$10 m s^{-1}. A similar estimate can be obtained by considering a parcel of a buoyant fluid and estimating pressure perturbations required to move the air above and below the parcel to allow the parcel to rise. Finally, vortical motions with velocity magnitudes of 10 m s^{-1} also imply pressure perturbations of $\sim$ 1 hPa within the vortex core. Computational example presented in the next section will substantiate these estimates. It follows that $\Delta p/p \sim 0.001$ for typical situations of small-scale atmospheric dynamics. Hence, as far as moist thermodynamics is concerned, pressure perturbations can be neglected compared to the potential temperature perturbations as it is typically done in anelastic models; see e.g., Lipps and Hemler (1982); Grabowski and Smolarkiewicz (1996), among many others.

However, neglecting pressure perturbations in moist thermodynamics cannot be universally valid. For instance, in a tornado, pressure perturbations can reach 100 hPa when the velocities reach 100 m s^{-1}, and then $\Delta p/p \sim 0.1$[1]. As far as larger-scale dynamics is concerned, temperature and hydrostatic pressure perturbations within midlatitude weather systems can be of the order of 10 K and 10 hPa. Their impact on moist thermodynamics would then be comparable according to (5). Thus, to extend the validity of the moist soundproof system to small-scale and mesoscale extreme events as well as into larger-scale dynamics (e.g., moist baroclinic waves), one should develop an approach to include pressure perturbations into moist thermodynamics.

Traditional thinking is that pressure perturbations obtained from the mass continuity

[1]Note that we put aside the issue whether the soundproof equations can accurately simulate such a flow in the first place. However, the Mach number squared, an appropriate parameter determining validity of the soundproof system, is $\sim$ 0.1 is such a case. This suggests that the soundproof solution may still be sufficiently accurate.

constraint via the associated elliptic pressure solver in the anelastic or pseudo-incompressible system should not be used in other parts of the model. This is because, for instance, anelastic model dynamics only care about pressure gradients, not the pressure magnitude, and the pressure is only known up to a constant. As will be illustrated by computational examples below, one can design a pressure solver in such a way that the pressure magnitude is predicted in addition to the pressure gradients and thus the pressure can be used in the moist thermodynamics. The key aspect concerns the formulation and application of the boundary conditions and specifics of the generalized Laplacian operator $\sim \nabla\cdot(\mathbf{C}\,\nabla\, p)$, where $\mathbf{C}$ represents the coefficient matrix; see the appendix for details.

For illustration, the next two sections compare idealized two-dimensional moist simulations performed with the EULAG model applying either anelastic or fully-compressible dynamics options. The anelastic moist EULAG model applies explicit thermodynamics (Grabowski and Smolarkiewicz 2002, and references therein). It is applied in either the original version, that is, with the perturbation pressure excluded from the moist thermodynamics (Lipps and Hemler 1982; Grabowski and Smolarkiewicz 1996) (referred to as the standard anelastic; ANES) or with the anelastic perturbation pressure combined with the input hydrostatically-balanced pressure profile and used in the moist thermodynamics (referred to as the generalized anelastic; ANEG). The compressible model (Smolarkiewicz and Szmelter 2009), referred to as COMP, solves equations of gas dynamics applying nonoscillatory forward-in-time integration scheme (Smolarkiewicz and Margolin 1997), very much alike the anelastic EULAG; cf. section 4 in Smolarkiewicz (2006) for discussion. Extension to moist processes includes replacing dry density by its moist counterpart, with the moist equation of state given by $p = \rho RT(1 + 0.61q_v)$, where ρ is the moist air density and q_v is the water vapor mixing ratio. The compressible model uses the acoustic time step required for numerical stability. This is impractical from the perspective of weather and climate, but leads to accurate compressible solutions, unobscured by numerical devices admitting long time steps in elastic models. Here compressible solutions are considered references for the anelastic models. The emphasis in the discussion will be on the comparison of the perturbation pressure between compressible and anelastic models because these perturbations are used in the moist thermodynamics. Applying the same numerical framework—the anelastic/compressible EULAG model—minimizes the influence of the numerics and better exposes differences in the theoretical model formulation.

4. Anelastic and compressible small-scale dynamics: moist thermals in stratified environment

a. Setup of simulations

The computational examples presented in this section address two-dimensional moist thermals rising from rest in a stratified environment, following Grabowski and Clark (1991, 1993a,b). A range of initial buoyancy perturbations is considered. The initial buoyancy perturbation combined with water-saturated initial conditions within the thermal leads to the rising motion accompanied by the condensation and latent heat release. As the thermal rises, shear and buoyancy gradients across the cloud-environment interface lead to the development of interfacial instabilities (entraining eddies) as discussed in Grabowski and Clark (1991, 1993a,b). These instabilities are sensitive to details of model numerics and can result in different flow realizations at later times; see, e.g., Figs. 2 and 3 in Grabowski and Smolarkiewicz (2002). To delay the onset of these instabilities, model physics includes explicit diffusion with a constant diffusion coefficient of 2.5 $m^2 s^{-1}$. Periodic lateral boundaries and rigid-lid lower and upper boundaries are assumed. As in simulations reported in section 3a of Grabowski and Smolarkiewicz (2002), a uniform 10-m gridlength is used in both horizontal and vertical directions.

The environment is assumed to have constant static stability of 1.3×10^{-5} m^{-1} and relative humidity of 20%, with the temperature and pressure of 283 K and 850 hPa at the lower boundary. The hydrostatically-balanced anelastic profiles of the potential temperature, pressure and density are prescribed as in Clark and Farley (1984, see Eq. 2 therein). The same initial profiles are also used in the compressible model, except for the density profile that is modified to include effects of moisture.

The circular initial temperature perturbation with 300 m radius is imposed in the middle of the 3.8×4 km^2 computational domain. The perturbation center is initially at the height of 800 m above the bottom boundary. The air within the 200 m radius is assumed saturated and the relative humidity smoothly decreases as in Grabowski and Clark (1991) over 100 m towards the 20% environmental relative humidity. The compressible model solves the continuity equation for the moist air density with the pressure derived from the predicted potential temperature and moist air density. Because of that, the initial density perturbation is derived from the moist equation of state at the onset of the compressible simulation. Three different initial potential temperature perturbations are considered: 0.5, 5 and 50 K. The first one may be considered typical for small convective clouds. The largest perturbation represents magnitude outside the range typical for atmospheric moist convection and is used here to expose differences between anelastic and compressible systems.

Table 1 shows comparison of model timesteps and total integration time for all simulations. A relative ratio of the anelastic and compressible timesteps for 0.5, 5, and 50 K simulations is 100, 25 and 1, respectively. The difference in total integration time is dominated by this ratio. Both models use the same timestep in the 50 K case, and the total integration time of the anelastic model is about 10% smaller than of the compressible model. This indicates that solving the elliptic problem for the pressure perturbation carries comparable cost to the advection of one additional field, the air density, in the compressible model.

b. Results

The large difference in the initial buoyancy perturbation for the three cases has a strong impact on the evolution of moist thermal in terms of the vertical velocity and the condensation rate evolutions. To better compare results with various initial perturbations, a non-dimensional buoyancy time scale T_b is introduced following Sanchez et al. (1989):

$$T_b = r_0(2gr_0\theta'/\bar{\theta})^{-1/2}, \tag{6}$$

where $r_0 = 300$ m is the initial radius of thermal, θ' is the initial potential temperature perturbation, $\bar{\theta} = 300$ K, and $g = 9.81\ \mathrm{m\,s^{-1}}$ is the gravity constant. The real time t is normalized by the buoyancy time scale T_b. The buoyancy time scale for the initial potential temperature perturbations of 0.5, 5, and 50 K is 95, 30, and 9.5 s, respectively.

In this paper, results are considered from only the first 10 t/T_b. This is because interfacial instabilities that develop at the leading edge of the thermal in all three cases begin to have a noticeable impact on the solution roughly at 5 t/T_b, and they dominate the solution after 10 t/T_b. As a consequence, gradual disintegration of the single convective structure and a formation of a variety of secondary circulations is simulated. The instabilities develop at scales determined by the characteristics of the leading edge interfacial layer, such as the shear and buoyancy gradient; see Grabowski and Clark (1991) for a detailed discussion. Test simulations with different values of the diffusion coefficient showed that adding explicit diffusion can only delay the development, but is not able to suppress it.

As an illustration of the above discussion, we show in Fig. 1 the total water fields from all nine simulations (three model formulations and three magnitudes of the initial perturbation) at the nondimensional time of 10 t/T_b. For the smallest initial perturbation, the solutions correspond to the dimensional time of about 16 min. The solutions are strongly affected by the explicit diffusion; see a diffused pattern of contours near the bottom of the thermal, especially when compared to the other solutions. Condensed water is only present in the central overshooting part of the initial perturbation — it represents late evolution of the interfacial instability — and this is where the solutions differ between compressible and anelastic models. Similar conclusions apply to the intermediate initial perturbation. However, since these are for dimensional time of around 5 min, the edges of the thermal remain relatively sharp. Solutions for the strongest initial perturbation correspond to only about 2 min of the thermal rise, and the interfacial instabilities seem to evolve in a surprisingly similar manner between all three model formulations. The only difference between the anelastic and compressible models is slightly slower rise of the compressible thermal as quantified in more detail in the subsequent analysis.

Based on results presented in Fig. 1, we show in Fig. 2 pressure perturbations at the nondimensional time of 5 t/T_b. The figure shows that pressure perturbations are dominated by pairs of counter-rotating vortices, with a reduced pressure within their centers, into which the initially circular buoyancy perturbations evolved. Positive pressure perturbations are found in front of the thermal as the thermal pushes upward through the initially motionless air. For each of the initial buoyancy perturbation, the anelastic solution in the left panel (i.e., ANES) agrees well with the compressible solution in terms of spatial structure and magnitude, the latter reaching minimum of about -6, -70 and -1000 Pa, respectively. The figure shows that the anelastic pressure perturbations compare well with the compressible solutions. The solutions based on the generalized anelastic model (ANEG) are shown in the middle column of Fig. 2. These results are practically identical to those from the standard anelastic model; this is consistent with the discussion in the previous section (cf. Eq. 5).

Figure 3 compares pattern of the vertical velocity at 5 t/T_b. Again, the differences are very small, except that the 50-K anelastic solution propagates slightly faster than the compressible one as evident from higher vertical velocities. This agrees with our experience with similar dry simulations where even larger temperature perturbations were considered and consequently larger deviations between compressible and anelastic solutions were simulated. Arguably, this is also consistent with a heuristic argument that larger buoyancy perturbations and thus stronger vertical velocities lead to more significant effects of air compressibility above the thermal that impede the thermal rise.

To further support above statements, time evolutions of the minimum and maximum pressure perturbations within the computational domain are shown in Fig. 4. Although pressure solutions from the compressible model presented in Fig. 2 are smooth, one should keep in mind that sound waves form an integral part of the solution. They are induced mostly by an upward movement of the density perturbation, but also by the continuous latent heat release inside the thermal. Sound waves propagate across the entire domain, reflect from model boundaries, and are responsible for the formation of the pressure perturbation field shown in Fig. 2. Their effect is clearly visible in Fig. 4, where compressible solutions feature oscillations with periods between 10 and 20 sec. The latter roughly agrees with the time needed for the sound waves to propagate across the computational domain. In order to reduce the impact of these waves, the compressible model employed divergence damping technique of Skamarock and Klemp (1992). Solutions without divergence damping were similar to those shown here, but with significantly larger oscillations in Fig. 4 and with small wiggles on the pressure perturbation isolines in Fig. 2. The key point is that compressible solutions tend to oscillate close to smooth anelastic solutions, perhaps with the exception of the solutions for the largest initial perturbation. The two anelastic solutions are practically indistinguishable for all cases considered.

Figure 5 shows evolutions of the height of the center of mass (barycenter) of the total water mixing ratio q_t and the maximum of the updraft strength. The total water was chosen because it is an invariant of the phase change and marks well the evolution of the initial moisture perturbation. For the smallest initial perturbation – slightly larger than in Grabowski and Clark (1991) where only initial humidity perturbation was considered — thermal approximately reaches the level of neutral buoyancy after about four nondimensional time units (i.e., around 400 s) and remains close to this altitude for the rest of the simulation. Maximum vertical velocities are around a few meters per second. Differences between compressible and anelastic solutions in the latter part of the simulations merely reflect different flow realizations due to interfacial instabilities as illustrated in Fig. 1. This is supported by a set of supplementary simulations with the anelastic model for a range of model timestep Δt. These simulations show that the differences between anelastic and compressible solutions decrease significantly with the decreasing difference in Δt. For instance, the difference in the q_t barycenter height after 10 t/T_b is 138 m for the 2 s anelastic timestep (cf. Fig. 5), but it decreases to 66 m for 0.2 s and 49 m for 0.02 s; the latter timestep is the same as in the compressible model. Moreover, anelastic simulations applying smaller timesteps result in solutions that loose their horizontal symmetry earlier. This suggests that the cumulative numerical (truncation plus round-off) errors have a considerable impact on a development of small-scale interfacial instabilities and thus on the overall behavior of a rising thermal. Therefore, one should keep in mind that the differences between compressible and anelastic solutions can be of various origins, with details of model numerics playing an important role in the comparison. This point is especially valid for simulations with weak forcing, when the difference between the forcing and the numerical noise is relatively small.

Solutions for the intermediate temperature perturbation in Fig. 5 are close to each other, with small differences apparent only in the last two nonodimensional time units (about one minute of the dimensional time) as illustrated in Fig. 1. For the largest initial perturbation, thermals rise about 10% faster in the anelastic model than in the compressible model, in agreement with the previous discussion. Differences in the maximum vertical velocity are initially small, 1-2 $\mathrm{m\,s^{-1}}$, and reach several $\mathrm{m\,s^{-1}}$ in the second half of the simulation. No significant difference between the two anelastic models are present regardless of the initial perturbation. The magnitude of simulated pressure perturbations (Fig. 4) are consistent with the maxima of the vertical velocity as argued in the previous section (i.e., ~ 10, ~ 100, and ~ 1000 Pa for the three initial perturbations).

The large perturbation of 50 K is used here to illustrate the limits of the anelastic approach, and only in this case the nonhydrostatic pressure perturbations have some (albeit still small) impact on the saturation adjustment. This is documented in Fig. 6 that shows the evolution of the maximum of the cloud water mixing ratio. The differences between anelastic and compressible solution for nondimensional times larger than two are consistent with the previous discussion (i.e., weaker updraft in the compressible case). Small differences between the two anelastic models are apparent as well. More interesting, however, are the differences during the initial two nondimensional time units, documented in the insert of the figure. The insert shows that the standard anelastic model underpredicts the amount of the cloud water by about 0.1 $\mathrm{g\,kg^{-1}}$, whereas the compressible and generalized anelastic model agree quite well. The latter is not true during the initial 0.1 of the nondimensional time, that is, during the initial approximately 1 s of the simulation time. The 1-s time corresponds to a period required by sound waves to propagate across the initial buoyancy perturbation to establish corresponding pressure perturbation in the compressible model. This happens instantaneously in the anelastic model.

5. Anelastic and compressible mesoscale dynamics: moist orographic flow

a. Setup of simulations

The second example considered in this study examines moist two-dimensional stratified flow over a bell-shaped mesoscale mountain. Experimental setup follows Grabowski and Smolarkiewicz (1996, GS96 hereinafter; see section 4b therein), with parameters exactly as in GS96 unless otherwise stated. As in simulations of the previous section, the moist thermodynamics is limited to the condensation/evaporation only. The height of the mountain is increased to $h = 1000$ m compared to GS96 to enhance orographically induced cloud water. The uniform inflow horizontal velocity of $U = 20\ \mathrm{ms^{-1}}$ is assumed to maintain similar to GS96 flow regime in terms of the Froude number $U/Nh \approx 3/2$. The relatively cool surface temperature of 273 K ensures absolute stability of the flow and eliminates potential instability which occurs when the equivalent potential temperature decreases with height in the lower troposphere due to the impact of water vapor (see section 6.7 in Emanuel 1994). All simulations apply the subgrid-scale turbulence scheme based on the the turbulent kinetic energy (Margolin et al. 1999). The domain size is 640×18 km^2 with horizontal and vertical gridlength of 2 km and 250 m, respectively. Anelastic/compressible models are integrated applying 10/0.5 s time step. Simulations are run for 6 hrs, sufficient to reach approximately steady-state solutions. The simulations require 49 and 667 s of the wallclock time when using 32 processors for the anelastic and compressible models, respectively.

As in the previous section, solutions from the three models are compared: the standard anelastic (ANES), the generalized anelastic (ANEG) and the fully-compressible (COMP). A significant difference from the rising thermal simulations of the previous section is that the orographic flow is differently affected by the round-off and truncation errors. More specifically, in the case of a rising moist thermal, these errors affected development of interfacial instabilities and had a strong impact on the flow at later times. Model results for a stable orographic flow with a steady-state solution (i.e., no convection) are affected predominantly by the model mathematical formulation and to a smaller degree by the model numerics.

b. Results

Figure 7 shows results for the three models, ANES, ANEG, and COMP, after 6 hours of the simulation. Only central 300 km of the horizontal domain is shown. The solution consists of two vertical wavelengths apparent in the fields of the pressure and potential temperature perturbations and the vertical velocity. Perturbations in the upper part of domain attenuate with height due to the presence of the gravity-wave absorber. The vertical velocity pattern is limited to the region directly above the topography (thus documenting the close-to-hydrostatic flow regime), with the pressure and potential temperature perturbations extending horizontally hundreds of kilometers. The patterns are almost identical regardless of the model considered. The two anelastic models provide almost the same solutions that compare well to the fully-compressible solution. Minor differences (around a single contour interval, i.e., ∼10 Pa) are simulated for the pressure perturbations in the upper part of the domain and away from the mountain. More detailed comparison of the anelastic and compressible pressure perturbations shows that the differences are mostly located in a narrow zone between 4 and 8 km right above the mountain, with extreme values as large as 20 Pa. This region is also characterized by a slight (0.1-0.2 K) underestimation of the potential temperature perturbation by the anelastic models. Cloud fields for all three simulations are very similar. The latter is consistent with the magnitude of temperature and pressure perturbations, up to 5 K and 2 hPa, that according to (5) imply only a small impact of pressure perturbations on the moist thermodynamics.

Table **??** shows the extreme values of the fields from Fig. 7 together with the extrema of the difference fields between the anelastic and compressible solutions. The maxima and minima of various fields differ little, typically 1 or 2%, with the largest differences for the maxima of the potential temperature perturbations (up to 4%). The extrema of the difference fields (ANES-COMP and ANEG-COMP) are significantly larger (in the absolute sense) than the differences in the extrema between ANES, ANEG, and COMP. This implies that the differences come from slightly different spatial patterns of model solutions rather than from under- or overprediction of the extreme values. Overall, the table provides no hint as to whether the generalized anelastic model provides solutions that are closer to the compressible model. For instance, the maximum cloud water mixing ratio is 1.037 $\mathrm{g\,kg^{-1}}$ for ANES and 1.049 $\mathrm{g\,kg^{-1}}$ for ANEG and COMP. But the extrema for other fields in the ANES solution are typically closer to COMP than the ANEG, and the cloud water seems to be an exception. Such an ambiguity is also supported by the extrema of the difference fields, with the extrema of the ANES-COMP smaller for some fields and larger for others than ANEG-COMP. Additional simulations of ANEG and ANES models with the same time step as used in the COMP model has not clarified the situation either. Overall, one can only conclude that the differences between various model formulations are small and difficult to explain, perhaps in agreement with the scaling suggested by Eq. 5.

Time series of the extreme values of pressure perturbations, the maximum of cloud water mixing ratio and the total mass of the condensed water ($\int \rho q_c \, dxdz$; in $\mathrm{kg\,m^{-1}}$) are shown in Figs. 8 and 9. The series demonstrate how the anelastic and compressible models approach their steady state solutions. Pressure fluctuations in the compressible solution are due to sound waves propagating horizontally across the domain. The amplitude of the oscillations decline with time, and after about 5 hours a solution close to the steady state is reached. The evolution of the maximum cloud water mixing ratio and the total condensed water mass show consistent differences between ANES and ANEG models as well as a better agreement between ANEG and COMP. The comparison between the three solutions at the early stage of simulation is highlighted by enlarged panels (a) and (b) in Fig. 9. These show that the generalized anelastic solution better follows the fully-compressible solution.

6. Summary and outlook

This paper seeks to advance theoretical methodologies and their efficient implementations for very-high-resolution nonhydrostatic simulation of the Earth's atmosphere general circulation with soundproof equations. Compressible dynamics is universally valid across the entire range of spatial and temporal scales (i.e., from small-scale turbulence to planetary circulations), but impose computational limitations that are difficult to overcome. Current community efforts focus on alternative forms of the governing equations for modeling large-scale dry atmospheric motions. Efficient numerical simulation of moist processes in very-high-resolution cloud-resolving general circulation models applying those alternative equations is an uncharted territory.

There is a significant experience in modeling moist processes at the opposite limits of the spatial scales involved (i.e., small-scale nonhydrostatic versus large-scale hydrostatic dynamics and thermodynamics). A practical approach suitable for multiscale simulation of weather and climate that combines experiences from large-scale and small-scale dynamics calls for unification of moist thermodynamics. We focus on an approach that applies potential temperature as the main thermodynamic variable because it is conserved in dry adiabatic motions. Alternative approaches, for instance, based on entropy concepts (i.e., the equivalent potential temperature) are deemed inappropriate because of the underlying thermodynamic equilibrium assumption, only approximately valid for water clouds and invalid for ice-bearing clouds. Moreover, semi-implicit integration of the governing equations (Smolarkiewicz 2011; Grabowski and Smolarkiewicz 2002) favor application of the potential temperature as the main thermodynamic variable.

The moist thermodynamics require local values of the temperature and pressure. The pressure field is needed not only in the formula for the saturated water vapor mixing ratio, but — more importantly — for the conversion of the potential temperature into temperature. In the soundproof system of equations, the key question is whether the pressure perturbations obtained from the elliptic pressure solver can be applied in the moist thermodynamics. In traditional small-scale soundproof models, pressure perturbations are typically neglected in the moist thermodynamics and only the environmental hydrostatic pressure profile is used (Lipps and Hemler 1982). A simple scaling argument shows that such an approach is appropriate for low-Mach-number small-scale flows. However, for flows with appreciable Mach numbers (e.g., ~ 0.1 or larger) pressure perturbations should be used in the moist thermodynamics. The same is true for larger-scale flows (e.g., midlatitude weather systems) where nearly-hydrostatic pressure perturbations may affect moist thermodynamics in a manner comparable to the potential temperature perturbations.

In support of the scaling argument, we compare model solutions to two idealized small-scale and mesoscale moist atmospheric flow problems (rising moist thermal and moist flow over topography, respectively) obtained with anelastic and fully-compressible flow solvers. The anelastic solver that includes pressure perturbations into moist thermodynamics is referred to as generalized anelastic. In agreement with the scaling argument, we document strong similarities between solutions obtained with the compressible, standard anelastic and generalized anelastic flow solvers. It thus follows that the pressure perturbations derived from the elliptic pressure solver in the soundproof system can be applied in the moist thermodynamics. We plan to further substantiate this conjecture by studying diverse cases of moist atmospheric flows for a range of scales and physical scenarios and compare moist solutions obtained with soundproof and fully-compressible options of the EULAG model. Results of such studies will be reported in forthcoming publications.

Acknowledgments.

This material is based upon work partially supported by the U.S. Department of Energy under Award Number DE-SC0006748. The views and opinions of the authors expressed herein do not necessarily state or reflect those of the U.S. Government or any agency thereof. WWG was also partially supported by the NSF Science and Technology Center for Multiscale Modeling of Atmospheric Processes (CMMAP), managed by Colorado State University under cooperative agreement ATM-0425247. PKS acknowledges partial support by the US NSF grant OCI-0904599 and by funding received from the European Research Council under the European Union's Seventh Framework Programme (FP7/2012/ERC Grant agreement no. 320375). National Center for Atmospheric Research is sponsored by the National Science Foundation.

APPENDIX

Conservativity of elliptic solver

A discrete anelastic elliptic pressure equation, at an arbitrary mesh point $\mathbf{x}_i$ and instant t^n, can be compactly written as

$$\frac{1}{\rho_o}\nabla\cdot\rho_o\big(\hat{\mathbf{u}}-\mathbf{C}\nabla\phi\big)=0\ . \tag{A1}$$

Here: $\rho_o=\rho_o(z)$ is the density of an anelastic reference state, defined by the hydrostatic balance and a constant nonnegative stratification; the differential operator ∇ is identifiable with the vector of primitive discrete spatial partial derivatives in a model code; and $\hat{\mathbf{u}}$ denotes the explicit counterpart of the velocity vector $\mathbf{u}$ at t^n. The $\mathbf{C}\nabla\phi$ term specifies the implicit complement of $\hat{\mathbf{u}}$ (such that $\mathbf{u}=\hat{\mathbf{u}}-\mathbf{C}\nabla\phi$), where $\mathbf{C}$ symbolizes a matrix of known coefficients, generally varying with i and n. The role of the implicit complement is to assure the anelastic mass continuity constraint $\nabla\cdot\rho_o\mathbf{u}=0$ for all $\mathbf{x}_i$ and t^n. At heart of the complement is the implicit potential $\phi\propto(p-p_e)/\rho_o$ — a density normalized pressure perturbation[2] with respect to an ambient pressure p_e, often (but not necessarily) coinciding with the anelastic reference pressure $p_o=p_o(z)$. Together with suitable boundary conditions and the integrability condition, (A1) forms the generalized Poisson boundary value problem for ϕ.

In anelastic models, natural and most common boundary conditions for ϕ are either periodic or Neumann. While the former are straightforward, the latter deserve a comment. A Dirichlet boundary condition for velocity, $\mathbf{n}\cdot\mathbf{u}|_B^n=\mathbf{n}\cdot\mathbf{u}_e$, imply Neumann condition $\mathbf{n}\cdot\mathbf{C}\nabla\phi|_B=\mathbf{n}\cdot(\hat{\mathbf{u}}-\mathbf{u}_e)|_B^n$ for ϕ; where subscript $_B$ refers to the boundary points, $\mathbf{u}_e(\mathbf{x},t)$ is a larger scale ambient flow that satisfies the anelastic mass continuity $\nabla\cdot\rho_o\mathbf{u}_e=0$, and $\mathbf{n}$ is

[2]The proportionality constant is a model time step or its fraction, depending on the details of numerics.

the outward unit normal to the boundary $\partial\Omega$ of the integration domain Ω. Such a design of the boundary conditions assures the integrability condition $\int_{\partial\Omega} \rho_o \mathbf{n} \cdot \mathbf{u}^n = 0$ for (A1), given $\int_{\partial\Omega} \rho_o \mathbf{n} \cdot \mathbf{u}_e = 0$.

In EULAG, the elliptic problem (A1) is effectively solved to a specified physically-motivated tolerance, $\parallel r_{\mathbf{u}} \parallel_\infty \equiv \parallel (\delta t/\rho_o) \nabla \cdot (\rho_o \mathbf{u}) \parallel_\infty \leq \varepsilon$, using the preconditioned generalized conjugate residual algorithm (GCR), an iterative nonsymmetric variational Krylov approach, reviewed recently in Smolarkiewicz and Szmelter (2011). Regardless of the complexity and details of the GCR, an archetype iteration for the problem (A1) may be viewed as

$$\phi^{k+1} = \phi^k + b^k r^k \ , \tag{A2}$$

where, $k = 0, .., N$ numbers the iterations while ϕ^k is a shorthand for the kth iterate of ϕ_i^n. Furthermore, r denotes the residual error, i.e., the actual value of the lhs of (A1) for ϕ^k, whereas b^k is a coefficient (constant at any given k) derived variationally by minimizing residual error of subsequent iteration(s). For either Dirichlet or Neumann boundaries, the recurrence relation (A2) implies, respectively,

$$\phi_B^{k+1} = \phi_B^k + b^k r_B^k \ , \tag{A3}$$

$$\mathbf{n} \cdot \mathbf{C} \nabla \phi^{k+1}|_B = \mathbf{n} \cdot \mathbf{C} \nabla \phi^k|_B + b^k \mathbf{n} \cdot \mathbf{C} \nabla \ r^k|_B \ , \tag{A4}$$

The recurrences (A3) or (A4) imply that if the boundary conditions were satisfied at the preceding iteration, they will be satisfied at the subsequent iteration, given that the respective boundary conditions for r or $\mathbf{C}\nabla r$ are homogeneous. Thus, to ensure the correct boundary conditions for ϕ throughout the iteration process, it is important to satisfy them from the outset, at the initialization of the iteration loop, and to maintain the equivalent homogeneous boundary conditions while computing directional vectors, residual errors, and solution-error estimates that enter advanced Krylov-subspace solvers; see Smolarkiewicz and Szmelter (2011) for an exposition.

In particular, calculating Neumann boundary condition for ϕ^0 from the ambient flow (as discussed above) assures the correct boundary conditions for all ϕ^k, given the corresponding gradient term $\mathbf{C}\nabla(.)$ of the residual error, directional vectors, etc., is set to zero at the boundaries. Furthermore, because (A3) amounts to

$$\rho_o \phi^{k+1} = \rho_o \phi^k + b^k \nabla \cdot (\rho_o \mathbf{u}^k) \ , \tag{A5}$$

its discrete volume integral

$$\int_\Omega \rho_o \phi^{k+1} = \int_\Omega \rho_o \phi^k + b^k \int_{\partial\Omega} \rho_o \mathbf{n} \cdot \mathbf{u}^k \tag{A6}$$

implies

$$\int_\Omega \rho \phi^{k+1} = \int_\Omega \rho \phi^k \ , \tag{A7}$$

because the constructed boundary condition for velocity assures zero total flux through the model boundary $\partial\Omega$. Thus, initializing the model with $\phi = 0$ at $t = 0$, assures that the volume integral of ϕ vanishes at all times, thus adding no constant to the solution of the elliptic pressure equation.

REFERENCES

Abiodun, B. J., W. J. Gutowski, A. A. Abatan, and J. M. Prusa, 2011: CAM-EULAG: A non-hydrostatic atmospheric climate model with grid stretching. *Acta Geophysica*, **59**, 1158–1166.

Abiodun, B. J., W. J. Gutowski, and J. M. Prusa, 2008a: Implementation of a non-hydrostatic, adaptive-grid dynamics core in CAM3. Part II: dynamical influences on ITCZ behavior and tropical precipitation. *Clim. Dyn.*, **31**, 811–822.

Abiodun, B. J., J. M. Prusa, and W. J. Gutowski, 2008b: Implementation of a non-hydrostatic, adaptive-grid dynamics core in CAM3. Part I: comparison of dynamics cores in aqua-planet simulations. *Clim. Dyn.*, **31**, 795–810.

Arakawa, A., 1975: Modeling clouds and cloud processes for use in climate models. *The Physical Basis of Climate and Climate Modelling*, GARP Publications Series, Vol. 16, 181–197 pp.

Arakawa, A. and C. Konor, 2009: Unification of the anelastic and quasi-hydrostatic systems of equations. *Mon. Wea. Rev.*, **137**, 710–726.

Bauer, L. A., 1908: The relation between potential temperature and entropy. *Phys. Rev. (Series I)*, **26**, 177–188.

Bryan, G. H., 2008: On the computation of pseudoadiabatic entropy and equivalent potential temperature. *Mon. Wea. Rev.*, **136**, 5239–5245.

Charney, J. G., 1979: *Carbon Dioxide and Climate: A Scientific Assessment.* National Academy Press, 33 pp.

Clark, T. L. and R. D. Farley, 1984: Severe downslope windstorm calculations in two and three spatial dimensions using anelastic interactive grid nesting: a possible mechanism for gustiness. *J. Atmos. Sci.*, **41**, 329–350.

Clark, T. L., W. D. Hall, and J. L. Coen, 1996: Source code documentation for the Clark-Hall cloud-scale model: Code version G3CH01. NCAR Technical Note, NCAR/TN-426+STR., 137 pp.

Davies, T., A. Staniforth, N. Wood, and J. Thuburn, 2003: Validity of anelastic and other equation sets as inferred from normal-mode analysis. *Q. J. R. Meteorol. Soc.*, **129**, 2761–2775.

Durran, D. R., 1989: Improving the anelastic approximation. *J. Atmos. Sci.*, **46**, 1453–1461.

Durran, D. R., 2008: A physically motivated approach for filtering acoustic waves from the equations governing compressible stratified flow. *J. Fluid Mech.*, **601**, 365–376.

Emanuel, K. A., 1994: *Atmospheric Convection*. Oxford University Press, 580 pp.

Grabowski, W. W., 1998: Toward cloud resolving modeling of large–scale tropical circulations: A simple cloud microphysics parameterization. *J. Atmos. Sci.*, **55**, 3283–3298.

Grabowski, W. W., 1999: A parameterization of cloud microphysics for long–term cloud–resolving modeling of tropical convection. *Atmos. Res.*, **52**, 17–41.

Grabowski, W. W. and T. L. Clark, 1991: Cloud-environment interface instability: Rising thermal calculations in two spatial dimensions. *J. Atmos. Sci.*, **48**, 527–546.

Grabowski, W. W. and T. L. Clark, 1993a: Cloud-environment interface instability. Part II: Extension to three spatial dimensions. *J. Atmos. Sci.*, **50**, 555–573.

Grabowski, W. W. and T. L. Clark, 1993b: Cloud-environment interface instability. Part III: Direct influence of environmental shear. *J. Atmos. Sci.*, **50**, 3821–3828.

Grabowski, W. W. and P. K. Smolarkiewicz, 1996: On two-time-level semi-lagrangian modeling of precipitating clouds. *Mon. Wea. Rev.*, **124**, 487–497.

Grabowski, W. W. and P. K. Smolarkiewicz, 1999: CRCP: A cloud resolving convection parameterization for modeling the tropical convecting atmosphere. *Physica D*, Special Issue: *Predictability: Quantifying Uncertainty in Models of Complex Phenomena*, 18th Annual Conference of the Center for Nonlinear Studies, Los Alamos, NM, USA, 11-15 May 1998, Vol. 133, 171–178.

Grabowski, W. W. and P. K. Smolarkiewicz, 2002: A multiscale anelastic model for meteorological research. *Mon. Wea. Rev.*, **130**, 939–956.

Hauf, T. and H. Hoeller, 1987: Entropy and potential temperature. *J. Atmos. Sci.*, **44**, 2887–2901.

Khairoutdinov, M. F. and D. A. Randall, 2001: A cloud resolving model as a cloud parameterization in the NCAR Community Climate System Model: Preliminary results. *Geophys. Res. Let.*, **28**, 3617–3620.

Klein, R., 2011: On the regime of validity of sound-proof model equations for atmospheric flows. *Proc. of the ECMWF Workshop on Non-hydrostatic Modelling,* 8-10 November, 2010, Reading, UK (available at http://ecmwf.int/publications/library/do/references/show?id=90056), 35–53.

Klein, R., U. Achatz, D. Bresch, O. M. Knio, and P. K. Smolarkiewicz, 2010: Regime of validity of soundproof atmospheric flow models. *J. Atmos. Sci.*, **67**, 3226–3237.

Klemp, J. B. and R. B. Wilhelmson, 1978: The simulation of three-dimensional convective storm dynamics. *J. Atmos. Sci.*, **35**, 1070–1096.

Lipps, F. B. and R. S. Hemler, 1982: A scale analysis of deep moist convection and some related numerical calculations. *J. Atmos. Sci.*, **39**, 1796–1816.

Lipps, F. B. and R. S. Hemler, 1986: Numerical simulation of deep tropical convection associated with large-scale convergence. *J. Atmos. Sci.*, **43**, 1796–1816.

Margolin, L., P. K. Smolarkiewicz, and Z. Sorbjan, 1999: Large-eddy simulations of convective boundary layers using nonoscillatory differencing. *Physica D*, **133**, 390–397.

Miller, M. J. and P. K. Smolarkiewicz, 2008: Special issue: "Predicting weather, climate and extreme events". *J. Comp. Phys.*, **227**, 3429–3730.

Miura, H., M. Satoh, H. Tomita, A. T. Noda, T. Nasuno, and S. Iga, 2007: A short-duration global cloud-resolving simulation with a realistic land and sea distribution. *Geophys. Res. Lett.*, **34**, L02 804,doi:10.1029/2006GL027 448.

Neale, R. B. and B. J. Hoskins, 2000a: A standard test for AGCMs including their physical parameterizations, I: The proposal. *Atmos. Sci. Lett.*, doi:10.1006/asle.2000.0019.

Neale, R. B. and B. J. Hoskins, 2000b: A standard test for AGCMs including their physical parameterizations, II: Results for the Met Office Model. *Atmos. Sci. Lett.*, doi:10.1006/asle.2000.0020.

Ogura, Y. and N. A. Phillips, 1962: Scale analysis of deep and shallow convection in the atmosphere. *J. Atmos. Sci.*, **19**, 173–179.

Palmer, T. N., F. J. Doblas-Reyes, A. Weisheimer, and M. J. Rodwell, 2008: Toward seamless prediction: Calibration of climate change projections using seasonal forecasts. *Bull. Amer. Meteor. Soc.*, **89**, 459–470.

Pauluis, O., 2008: Thermodynamic consistency of the anelastic approximation for a moist atmosphere. *J. Atmos. Sci.*, **65**, 2719–2729.

Prusa, J. M. and P. K. Smolarkiewicz, 2003: An all-scale anelastic model for geophysical flows: dynamic grid deformation. *J. Comput. Phys.*, **190**, 601–622.

Prusa, J. M., P. K. Smolarkiewicz, and A. A. Wyszogrodzki, 2008: Eulag, a computational model for multiscale flows. *Comput. Fluids*, **37**, 1193–1207.

Randall, D. A., 2010: The evolution of complexity in general circulation models. *In The Development of Atmospheric General Circulation Models. Complexity, Synthesis and Computation.,* Edited by L. Donner, W. Schubert, and R. Somerville, Cambridge University Press, pp. 272.

Randall, D. A., M. Khairoutdinov, A. Arakawa, and W. Grabowski, 2003: Breaking the cloud-parameterization deadlock. *Bull. Amer. Meteor. Soc.*, **84**, 1547–1564.

Sanchez, O., D. J. Raymond, L. Libersky, and A. G. Petschek, 1989: The development of thermals from rest. *J. Atmos. Sci.*, **46**, 2280–2292.

Shukla, J., 1998: Predictability in the midst of chaos: A scientific basis for climate forecasting. *Science*, **282**, 728–731.

Shukla, J., 2009: Seamless prediction of weather and climate: A new paradigm for modeling and prediction research. *Science and Technology Infusion Climate Bulletin. Available at http://www.nws.noaa.gov/ost/climate/STIP/FY09CTBSeminars/shukla_021009.htm.*

Skamarock, W. C. and J. B. Klemp, 1992: The stability of time-split numerical methods for the hydrostatic and the nonhydrostatic elastic equations. *Mon. Wea. Rev.*, **120**, 2109–2127.

Smolarkiewicz, P. K., 2006: Multidimensional positive definite advection transport algorithm: an overview. *Int. J. Numer. Meth. Fluids*, **50**, 1123–1144.

Smolarkiewicz, P. K., 2011: Modeling atmospheric circulations with soundproof equations. *Proc. of the ECMWF Workshop on Nonhydrostatic Modelling,* 8-10 November, 2010, Reading, UK (available at http://ecmwf.int/publications/library/do/references/show?id=90054), 1–15.

Smolarkiewicz, P. K. and L. G. Margolin, 1997: On forward-in-time differencing for fluids: An Eulerian/semi-Lagrangian nonhydrostatic model for stratified flows. *Atmos.-Ocean Special*, **35**, 127–152.

Smolarkiewicz, P. K., L. G. Margolin, and A. Wyszogrodzki, 2001: A class of nonhydrostatic global models. *J. Atmos. Sci.*, **58**, 349–364.

Smolarkiewicz, P. K. and J. Szmelter, 2009: Iterated upwind schemes for gas dynamics. *J. Comput. Phys.*, **228**, 33–54.

Smolarkiewicz, P. K. and J. Szmelter, 2011: A nonhydrostatic unstructured-mesh soundproof model for simulation of internal gravity waves. *Acta Geophysica*, **59**, 1109–1134.

Szmelter, J. and P. K. Smolarkiewicz, 2010a: An edge-based unstructured mesh discretisation in geospherical framework. *J. Comput. Phys.*, **229**, 4480–4495.

Szmelter, J. and P. K. Smolarkiewicz, 2010b: An edge-based unstructured mesh framework for atmospheric flows. *Comput. Fluids*, **46**, 455–460.

Tapp, M. C. and P. W. White, 1976: A non-hydrostatic mesoscale model. *Quarterly Journal of the Royal Meteorological Society*, **102**, 277–296.

Wedi, N. and P. K. Smolarkiewicz, 2004: Extending Gal-Chen & Somerville terrain-following coordinate transformation on time-dependent curvilinear boundaries. *J. Comput. Phys.*, **193**, 1–20.

Ziemianski, M. Z., M. J. Kurowski, Z. P. Piotrowski, B. Rosa, and O. Fuhrer, 2011: Toward very high resolution NWP over Alps: Influence of the increasing model resolution on the flow pattern. *Acta Geophysica*, **59**, 1205–1235.

List of Tables

Table 1. Model timesteps Δt and the total integration times (run times) using 32 processors for the anelastic and compressible rising thermal simulations.

MODEL	EXPERIMENT					
	$\theta' = 0.5$ K		$\theta' = 5$ K		$\theta' = 50$ K	
	Δt [s]	run time [s]	Δt [s]	run time [s]	Δt [s]	run time [s]
anelastic	2	69	0.5	74	0.02	369
compressible	0.02	4992	0.02	1135	0.02	404

TABLE 2. Minima and maxima of the pressure perturbations (p'), vertical velocity(w), cloud water mixing ratio (q_c) and potential temperature perturbations (θ') for the orographic flow solutions obtained with ANES, ANEG, and COMP models after 6 hours. Bottom two rows show minima and maxima of the difference fields ANES-COMP and ANEG-COMP.

	p' [Pa]		w [$\mathrm{m\,s^{-1}}$]		q_c [$\mathrm{g\,kg^{-1}}$]		θ' [K]	
	min	max	min	max	min	max	min	max
ANES	-259.8	91.2	-2.54	2.83	0	1.037	-5.14	5.09
ANEG	-258.1	91.1	-2.53	2.81	0	1.049	-5.10	5.03
COMP	-252.4	92.0	-2.62	2.86	0	1.049	-5.17	5.25
ANES-COMP	-21.2	11.8	-0.15	0.13	-0.07	0.02	-0.32	0.32
ANEG-COMP	-23.2	12.4	-0.16	0.13	-0.07	0.02	-0.31	0.36

List of Figures

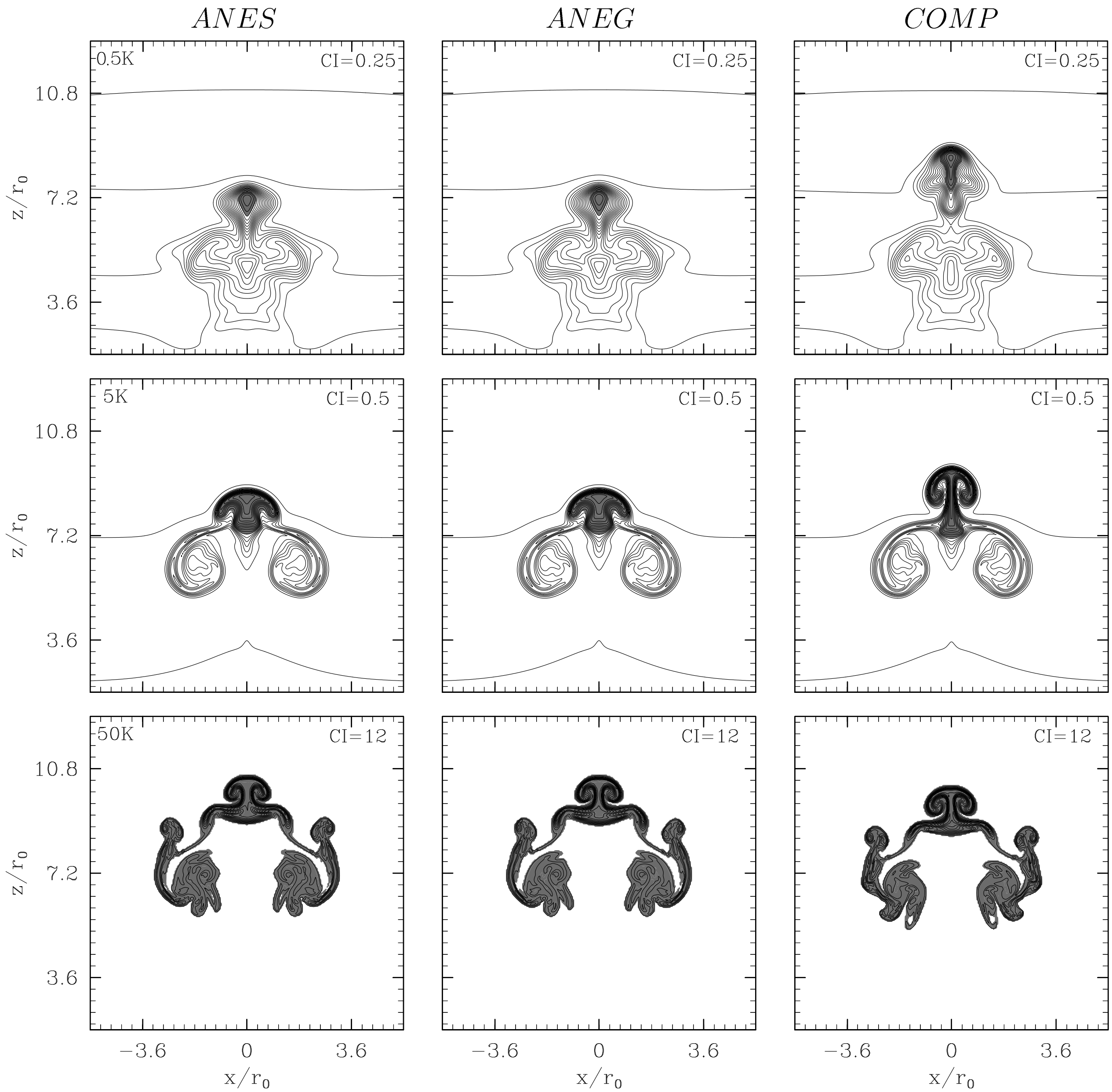

FIG. 1. Total water mixing ratio at 10 t/T_d for 0.5 K (upper row), 5 K (middle row) and 50 K (bottom row) for ANES (left column), ANEG (middle column) and COMP (right column). Regions of cloud water mixing ratio greater than 0.01 g kg^{-1} are shaded. Contour interval (CI; in g kg^{-1}) is shown in the upper right corner of each panel.

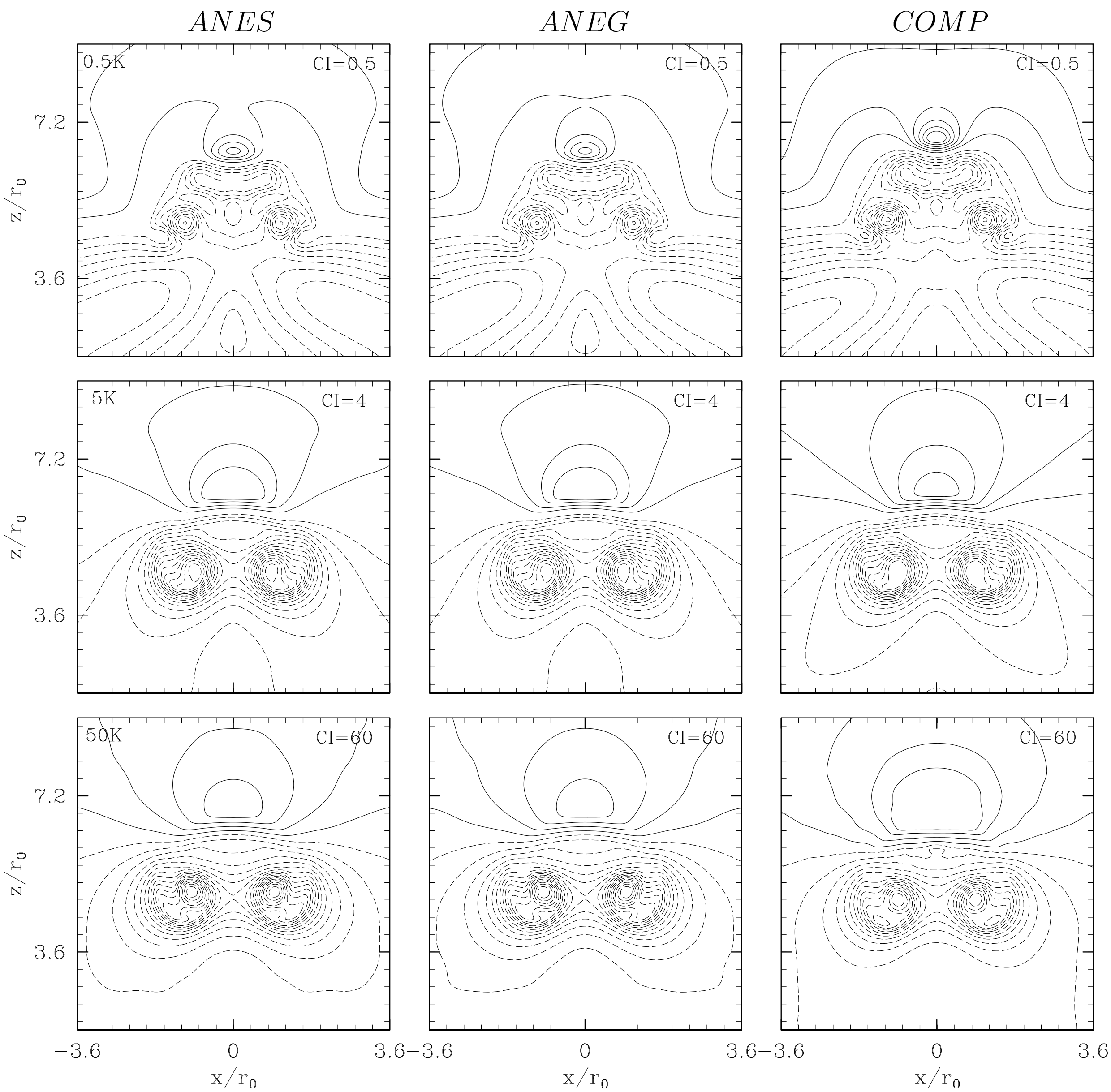

FIG. 2. Pressure perturbations at 5 t/T_b for 0.5 K (upper row), 5 K (middle row) and 50 K (bottom row) of the initial potential temperature perturbation. Left, middle, and right columns show results for ANES, ANEG, and COMP, respectively. Contour interval (CI; in Pa) is shown in the upper right corner of each panel.

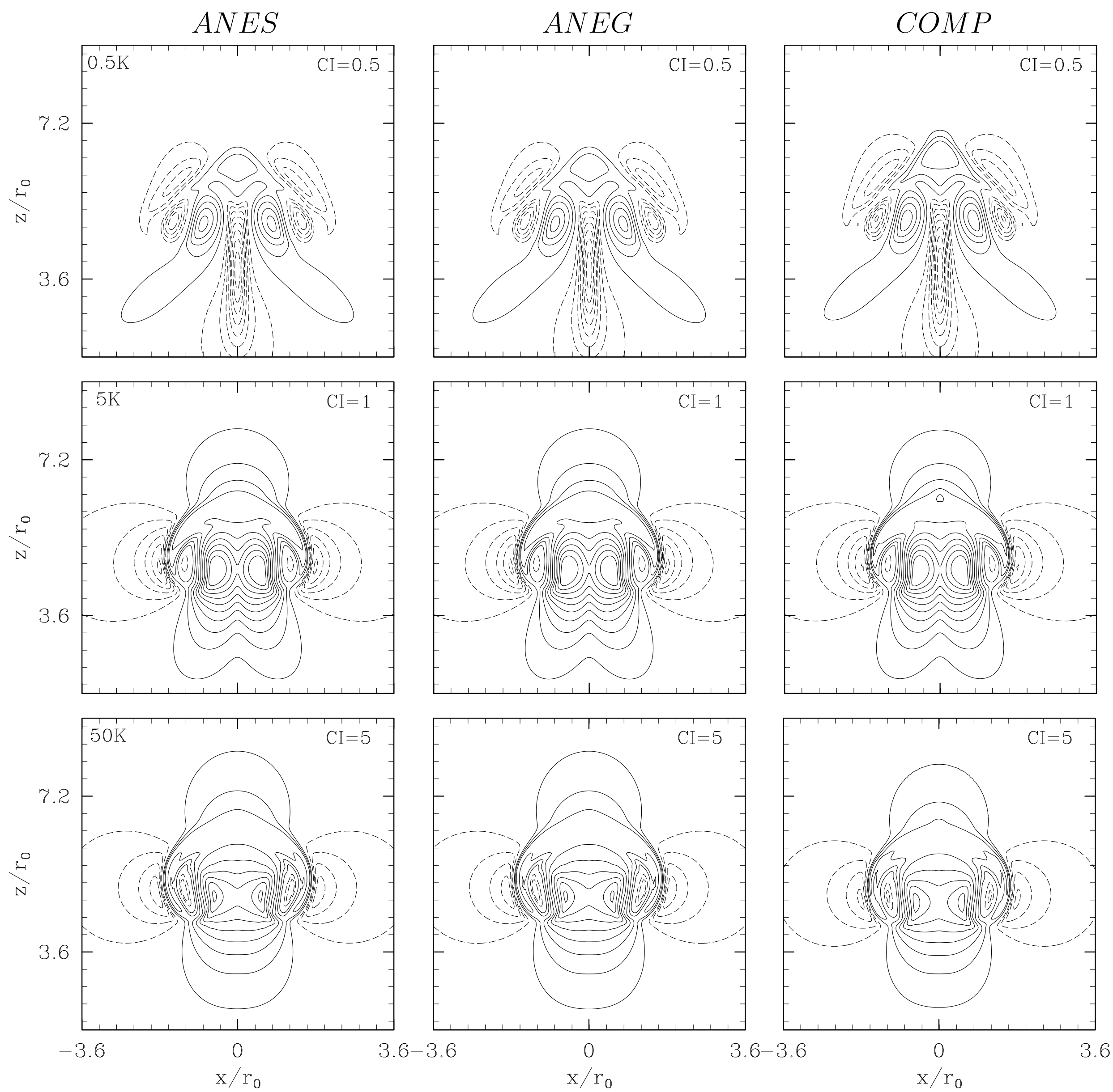

FIG. 3. As in Fig. 2, but for the vertical velocity field. Contour interval (CI; in $\mathrm{m\,s^{-1}}$) is shown in the upper right corner of each panel.

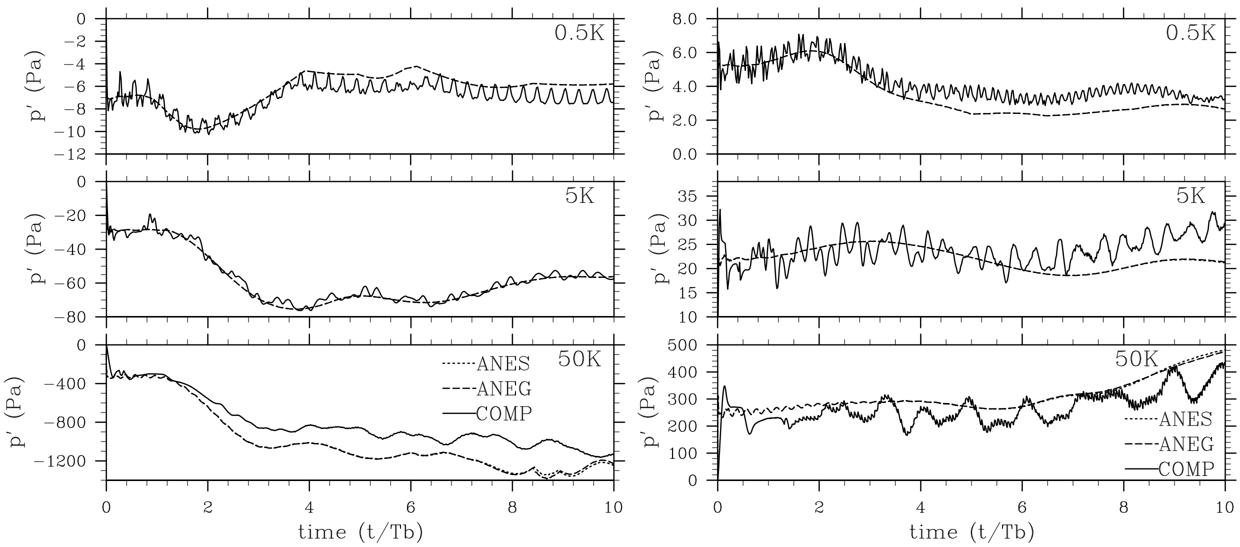

FIG. 4. Evolution of the minimum (left column) and maximum (right column) pressure perturbation for rising thermal simulations with different initial potential temperature perturbation: 0.5 K (upper row), 5 K (middle row), and 50 K (bottom row). ANES and ANEG solutions are almost indistinguishable.

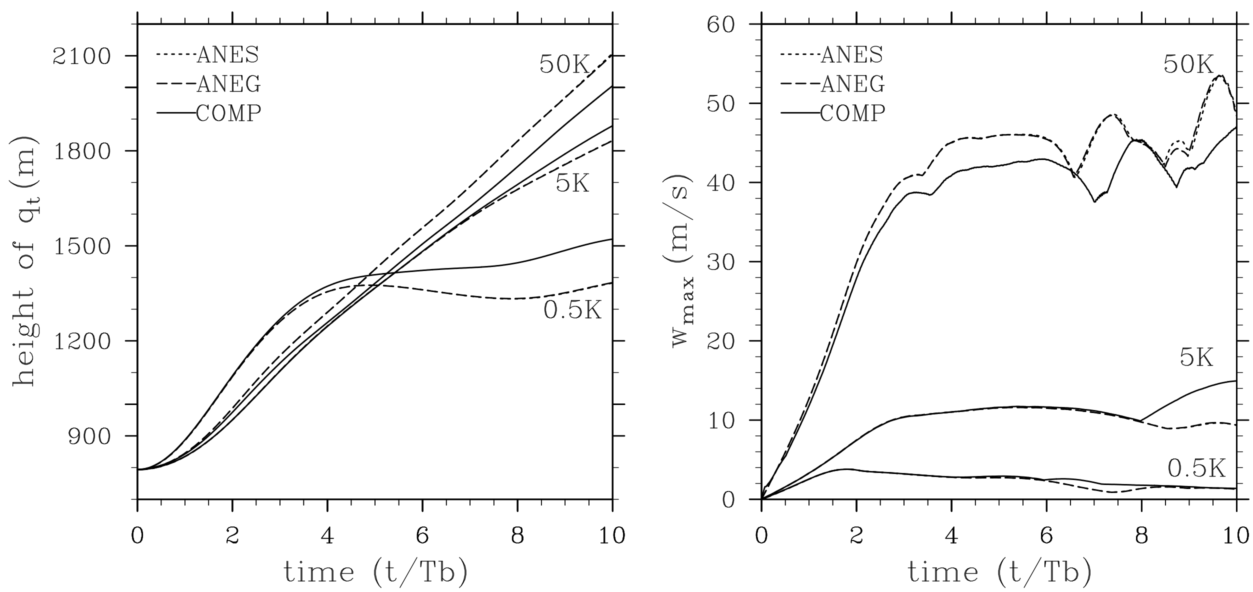

FIG. 5. Evolutions of the height of the total water mixing ratio barycenter (left panel) and the maximum vertical velocity (right panel) for rising thermal simulations with the three different initial potential temperature perturbations.

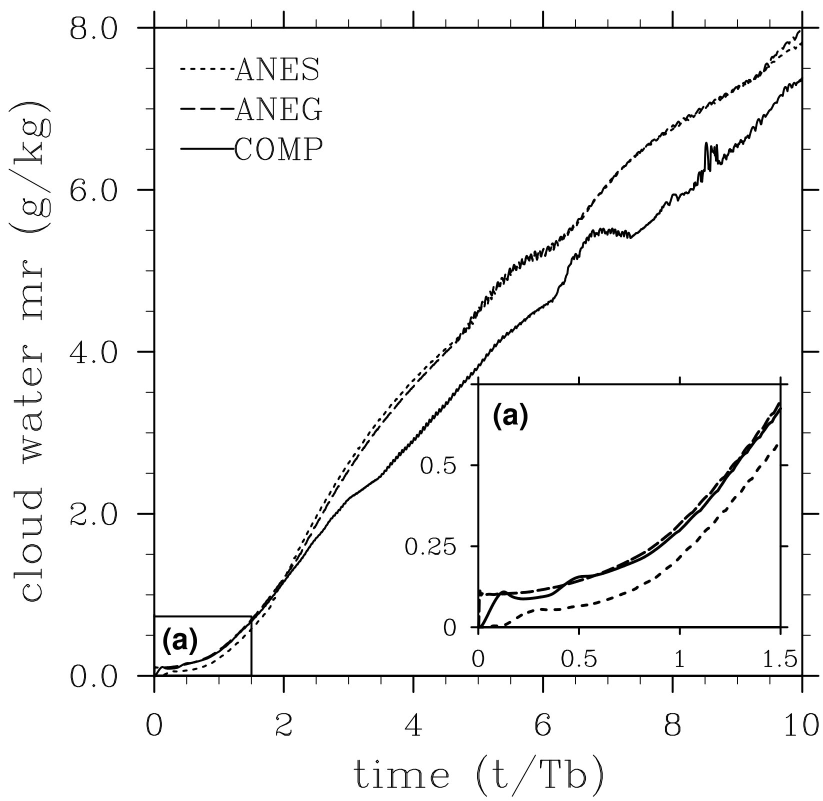

FIG. 6. Evolution of the cloud water mixing ratio maxima for rising thermal simulations with the initial potential temperature perturbation of 50 K. The insert (a) shows enlarged evolution during the first 1.5 unit of time. See text for a discussion.

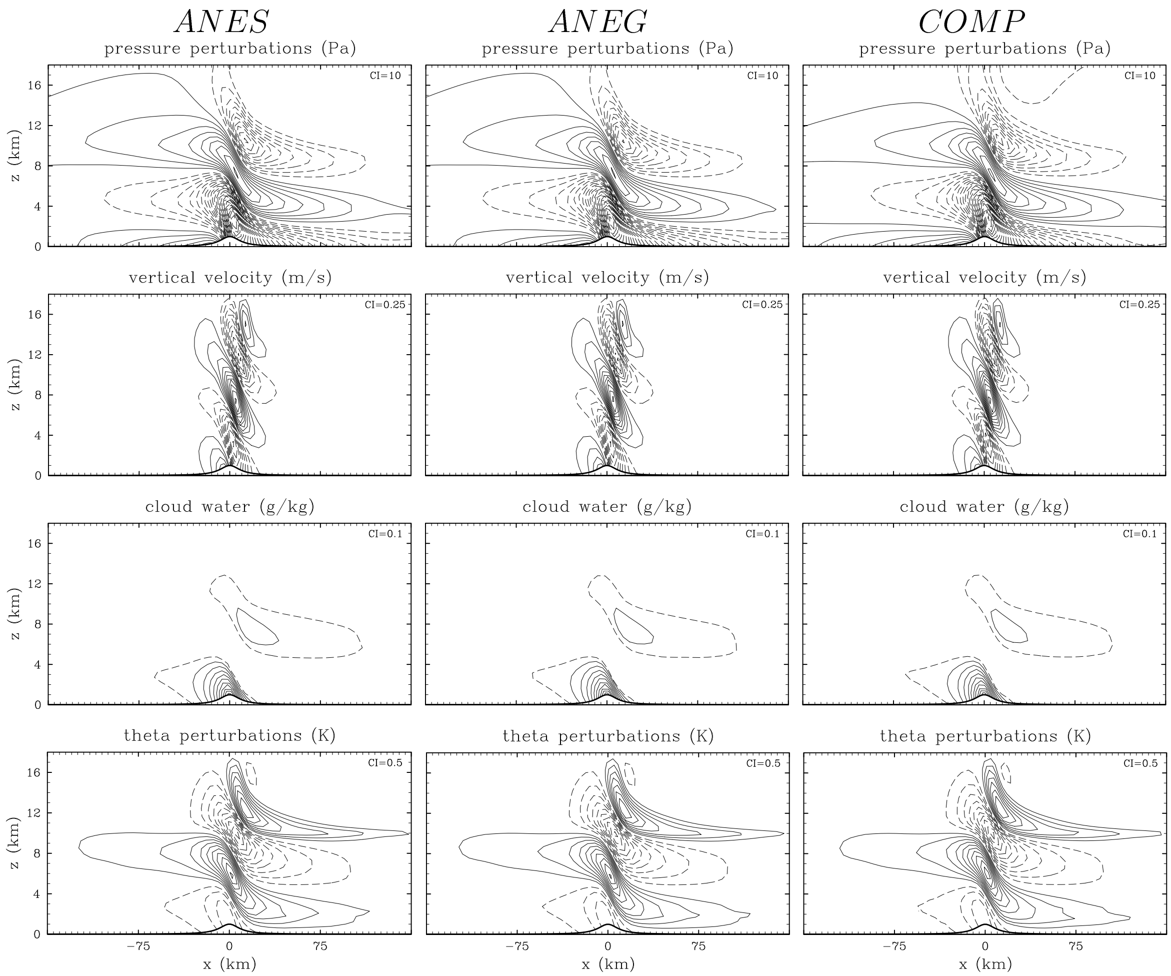

Fig. 7. Pressure perturbation (upper row), vertical velocity (2nd row), cloud water mixing ratio (3rd row) and potential temperature (bottom row) at hour 6 of the moist flow over mesoscale topography. Left, middle, and right columns show results for ANES, ANEG, and COMP, respectively. Contour intervals (CI) are shown in the right upper corner of each plot. The dashed line in the cloud water panels represents isoline of 0.01 $\mathrm{g\,kg^{-1}}$.

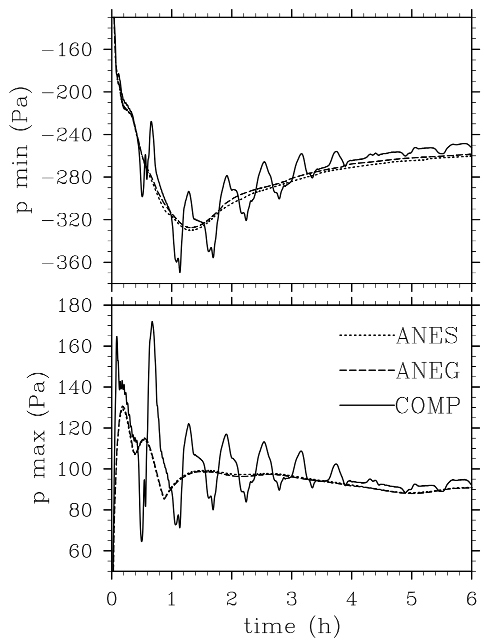

FIG. 8. Evolution of the minimum (upper panel) and maximum (lower panel) of the pressure perturbations for ANES, ANEG and COMP orographic flow simulations.

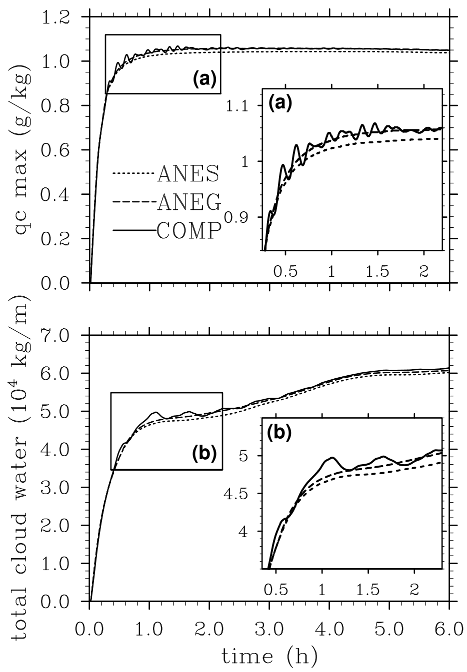

Fig. 9. Evolution of the maximum of the cloud water mixing ratio (upper panel) and total liquid water mass (lower panel) for ANES, ANEG and COMP orographic flow simulations. The inserts (a) and (b) show enlarged evolution during the model spinup. See text for a discussion.